

Monte Carlo Simulations of Thermal Conductivity in Nanoporous Si Membranes

STEFANIE WOLF,^{1,3} NEOPHYTOS NEOPHYTOU,^{1,2,4}
ZLATAN STANOJEVIC,^{1,5} and HANS KOSINA,^{1,6}

1.—Institute for Microelectronics, Technical University of Vienna, Vienna, Austria. 2.—School of Engineering, University of Warwick, Coventry CV4 7AL, UK. 3.—e-mail: wolf@iue.tuwien.ac.at. 4.—e-mail: neophytou@iue.tuwien.ac.at. 5.—e-mail: stanojevic@iue.tuwien.ac.at. 6.—e-mail: kosina@iue.tuwien.ac.at

We present a Monte Carlo study of heat transport in Si nanomeshes. Phonons are treated semiclassically as particles of specific energy and velocity that undergo phonon–phonon scattering and boundary scattering on the surfaces of the nanomesh pores. We investigate the influence of: (1) geometric parameters such as the pore arrangement/randomness and porosity, and (2) the roughness amplitude of the pore surfaces on the thermal conductivity of the nanomeshes. We show that the nanomesh porosity has a strong detrimental influence on the thermal conductivity. Boundary roughness still degrades the thermal conductivity, but its influence is smaller.

Key words: Phonon, Boltzmann transport equation, Monte Carlo, nanoporous silicon, nanomesh, thermoelectrics

INTRODUCTION

Nanoporous membranes made of single-crystalline Si (referred to as nanomeshes)^{1–3} are promising candidates for thermoelectric materials as they can provide extremely low thermal conductivity, κ , relatively high thermoelectric power factors, and the structure stability that other low-dimensional systems are lacking. Since Si is an abundant, non-toxic material with well-established manufacturing processes, such structures, once optimized, could provide the feasibility of large-scale applications. Recently, room temperature ZT values up to 0.4 were demonstrated in nanomeshes, a large increase compared to bulk $ZT_{\text{bulk}} \sim 0.01$.² To understand the parameters which determine the thermal conductivity in nanomeshes, involved simulation work is required. In this work, we calculate the thermal conductivity of nanoporous single crystalline Si membranes by solving the Boltzmann transport equation (BTE) for phonons using the Monte Carlo (MC) method.^{4,5} We describe the theoretical methodology, and examine the influence of geometry including pore arrangement (rectangular, hexagonal, random) and

material porosity, as well as the influence of boundary scattering on the thermal conductivity. We show that the material porosity strongly affects the thermal conductivity. Boundary scattering also affects the thermal conductivity, but its effect is weaker.

THEORY

The geometry of the devices is defined and a tetrahedral simulation grid is created using the ‘global TCAD solutions’ (GTS) framework.⁶ The devices consist of a simulation domain (channel) and two thermal contacts, i.e. a heat source and a heat sink which act as black bodies. The MC technique is described in detail in Refs. 4 and 5 with the difference that we use a single-particle scheme, meaning that only one phonon is simulated at each time. Each separate phonon is traced from its initialization in the contacts, through its drift in the channel, and finally up to its thermalization in the contacts. The MC algorithm accounts for longitudinal acoustic (LA) and transversal acoustic (TA) polarizations and nonlinear dispersion relationships. As shown in Fig. 1, following the work of Ref. 7, we use $\omega(k) = v_s k + ck^2$ as a fit for the bulk dispersion relationship under the isotropic Brillouin zone

(Received October 21, 2013; accepted July 8, 2014;
published online August 8, 2014)

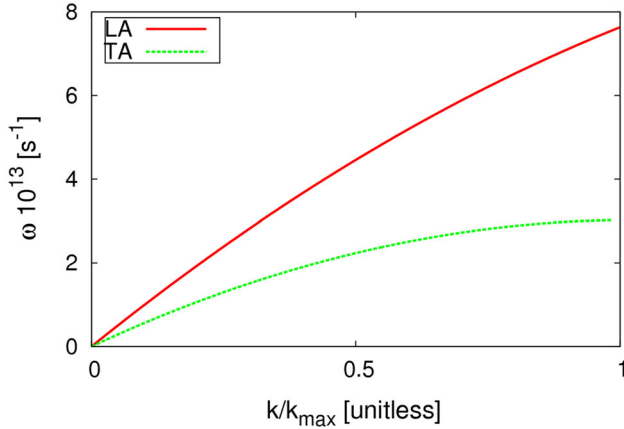


Fig. 1. Dispersion relationships for longitudinal acoustic (LA) phonons (red), and transversal acoustic (TA) phonons (green) (Color figure online).

approximation, where k is the wave vector norm and v_s and c are fitting parameters to match the thermal conductivity of bulk Si in the [100] direction. These dispersion coefficients are taken from Ref. 7 as $v_s = 9.01 \times 10^3$ m/s and $c = -2 \times 10^{-7}$ m²/s for the LA branch, and $v_s = 5.23 \times 10^3$ m/s and $c = -2.26 \times 10^{-7}$ m²/s for the TA branch.

The simulation steps are as follows. A phonon is initialized at a random position in the contacts according to the local temperature T . Initialization involves sampling of the phonon frequency, wave-vector, polarization and group velocity. The group velocity is defined as the slope of the dispersion relationship and is co-directional with the wave-vector. The phonon is injected in the channel and alternates between free flight and scattering events. During the free flight phase, phonons move linearly in time. Boundary scattering does not change the phonon frequency, but only its direction. In order to implement surface roughness, we use a constant specularity parameter p ranging from 0 to 1 to treat specular or diffusive boundary scattering, respectively. If a phonon reaches a device boundary, a random number $0 < R < 1$ is drawn. If $R > p$, then the phonon direction is randomly reset, otherwise the phonon is specularly reflected.

Three-phonon scattering is treated using phonon lifetimes as functions of frequency and temperature T for both polarization branches as described in Ref. 8:

$$\tau_{LA}^{-1} = B_{NU}^{LA} \omega^2 T^3 \quad (1a)$$

$$\tau_{TA,N}^{-1} = B_{NU}^{TA} \omega T^4 \quad (1b)$$

$$\tau_{TA,U}^{-1} = \begin{cases} 0 & \text{for } \omega < \omega_{1/2} \\ B_U^{TA} \omega^2 / \sinh\left(\frac{\hbar\omega}{k_B T}\right) & \text{for } \omega \geq \omega_{1/2} \end{cases} \quad (1c)$$

where N represents the normal and U the Umklapp processes, $\omega_{1/2}$ is the frequency corresponding to $k = k_{\max}/2$ and $B_{NU}^{LA} = 2 \times 10^{-24}$ s/K³, $B_N^{TA} = 9.3 \times$

10^{-13} K⁻⁴ and $B_U^{TA} = 5.5 \times 10^{-18}$ s taken from Ref. 8. After a three-phonon scattering event, the phonon frequency and direction is reset, whereas after a normal process the frequency and the magnitude of the wavevector and velocity are reset, following the scheme described in Ref. 5. Since we use a single-phonon simulation approach, when updating the phonon energy, in order not to violate energy conservation, we add the energy difference to the energy of the simulation domain cell in which the scattering event has taken place. Thus, the cell energy and temperature are modified accordingly.⁵ If the phonon reaches the outward boundary at the thermal contacts, it is absorbed and the simulation continues with a newly created phonon. This sequence is repeated until the cell temperature difference between iterations is below the error tolerance. After reaching steady-state (a linear temperature gradient is established between the hot and cold ends), we calculate the heat flux by sequentially injecting a prescribed number of phonons (N) from the source into the device. This is done one phonon at a time, and the typical number of phonons used is $N \sim 4 \times 10^6$. Our simulations indicate that it is enough to provide a convergence in the calculation of thermal conductivity. We sum the phonons' incident energy to E_{in}^H . As the phonons travel through the device, they engage in three-phonon scattering which can alter their frequency and direction. The energy of all back-scattered phonons (leaving the device through the source contact) is summed up to E_{out}^H . Additionally, we calculate the average time that it takes for a phonon to travel the distance through the device [time-of-flight (TOF)]. Then, we repeat the procedure by initializing phonons from the heat sink (cold end) and calculate E_{in}^C and E_{out}^C . The phonon flux is then given by $F = N_{tot} \frac{(E_{in}^H - E_{out}^H) - (E_{in}^C - E_{out}^C)}{N \langle \text{TOF} \rangle}$, where N_{tot} is the total number of phonons inside the device. The thermal conductivity is calculated using the heat flux through the medium for a given thermal gradient ∇T by applying Fourier's law as $\kappa = F/\nabla T$. The size of the devices we consider is $100 \text{ nm} \times 500 \text{ nm} \times 1 \mu\text{m}$, and the simulation time for the thermal conductivity of each device is around 8 h on a single central processing unit (CPU).

Note that the single-phonon approach we follow differs from the multi-phonon approaches described in the literature. In the multi-phonon approaches, a certain number of phonons are initialized at once according to the Bose-Einstein distribution and injected into the channel. The trajectories of all phonons are traced simultaneously at every time step, Δt , and the energy and temperature of all cells are also updated every Δt . The net flux upon convergence is computed at any interface perpendicular to the transport direction simply by calculating the net rate at which phonons cross that interface. In our single phonon approach, however, since we do not have access to all phonons travelling in the

channel at all times, the flux is calculated by determining the average flux due to one phonon crossing the entire domain, and then multiplying by the total number of phonons, as described above. While initially (before steady state) this approach does not correspond to the real physical situation in which multiple phonons travel simultaneously across the channel, at steady state it works as expected. The main advantage of the single-particle scheme is that it requires much less memory as it keeps track of only one phonon at a time, which is beneficial in complex structures such as the ones we consider, where the number of cells N_{cells} can reach very large numbers.

The simulator is initially calibrated to the measured thermal conductivity of bulk Si between 50 K and 500 K as shown in Fig. 2. For the bulk calibration, after the MC simulation, an important post-processing step related to the mean-free-path (MFP) needs to be performed. Low wavevector, k , (or long wavelength) phonons dominate transport, or at least control a large part of it, especially at low temperatures. The MFPs of these phonons can be much larger than the simulated device length, which is $1\ \mu\text{m}$ for the devices we consider.⁹ The limited domain length, therefore, imposes an additional series resistance on the flow of these phonons. For a correct comparison of our results to bulk Si measurements, in which case the dimensions are infinitely long, the simulated thermal conductivity needs to be scaled as described in Refs. 9 and 10 by $\kappa_{\text{bulk}} = \kappa_L (L + \lambda)/L$, where κ_L is the calculated thermal conductivity, L is the channel length, and λ is the bulk phonon MFP at a specific temperature taken from Ref. 9. κ_{bulk} will then be the resultant thermal conductivity, the one to be compared to the bulk measurements. This method essentially removes the contact series resistance from the MC calculation results. This scaling step is particularly important for bulk calibration in finite domain simulation of phonons, because the MFPs of phonons in Si vary from several micrometers (even up to millimeters) for low frequencies, to 100 s of nanometers around the frequencies in the middle of the spectrum, down to nanometers for high frequencies.¹¹ As shown by Jeong et al.,⁹ in bulk Si more than 50% of the heat is carried by phonons with MFPs longer than $1\ \mu\text{m}$, with the average phonon MFP at room temperature being $\sim 132\ \text{nm}$. Therefore, those long MFP phonons that carry more than 50% of the heat are strongly affected by the finite size of our domain. Note that this scaling is only relevant for the calibration to bulk data, whereas it is not needed for the simulation of nanomeshes since in that case the MFP is dominated by the pores in the channel, and the influence of the finite domain length is small.

In general, our results (red line) are in good agreement with measured bulk data (green line), and the simulations by Lacroix et al.⁵ (black triangles), as shown in Fig. 2. Our results slightly

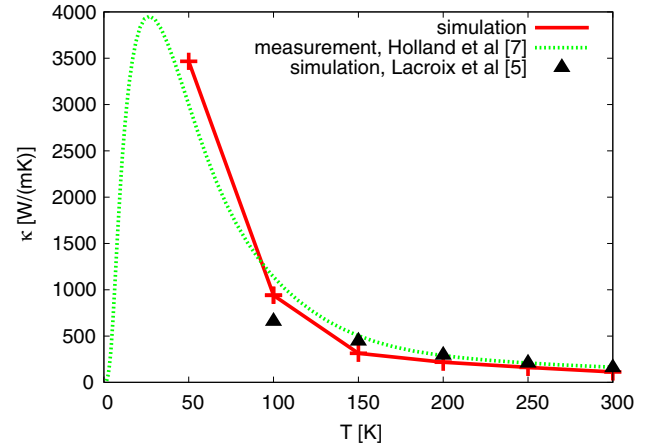


Fig. 2. Thermal conductivity of bulk Si. Measurements are shown in green. Simulations results from Ref. 5 are shown by the black triangles. Simulation results of this work are shown in red (Color figure online).

underestimate the thermal conductivity at temperatures above 100 K, (at room temperature, we achieve $\kappa = 113\ \text{W/mK}$ compared to $\kappa = 140\ \text{W/mK}$ for bulk Si). Several reasons might be responsible for this, i.e. the rather simplified band structure model, the simplified scaling of the long wavelength phonons, and possible inaccuracies in the MFPs provided in Ref. 9 (or inaccuracies caused by us in the extraction of those MFPs), but also the finite domain length of the simulation again, since we observe increasing thermal conductivity values as we increase the channel length from $1\ \mu\text{m}$ to $5\ \mu\text{m}$. However, we do not expect this deviation to affect the calculation results for the nanomeshes qualitatively or quantitatively, as the MFP in that case is limited by the pores in the material and not by the length of the simulation domain.

RESULTS AND DISCUSSION

We calculate the thermal conductivity in nanomeshes of three different hole arrangements: rectangular, hexagonal, and random. Figure 3 shows examples of the simulated device geometries, including examples of as much as 100 phonon trajectories in each structure. An interesting effect can be observed in the phonon trajectories. Although the motion of phonons is randomized in the randomized pore geometries (Fig. 3c), there is evidence that this is not the case in the rectangular and hexagonal geometries. Instead, preferential phonon paths exist in the rectangular (Fig. 3a) and hexagonal structures (Fig. 3b). In the case of rectangular structures, phonons tend to follow straight paths, whereas, in the hexagonal devices, phonons tend to follow diagonal paths, which are the directions of least phonon resistance. As we will discuss below, since the rectangular geometry provides paths of least resistance along the phonon transport

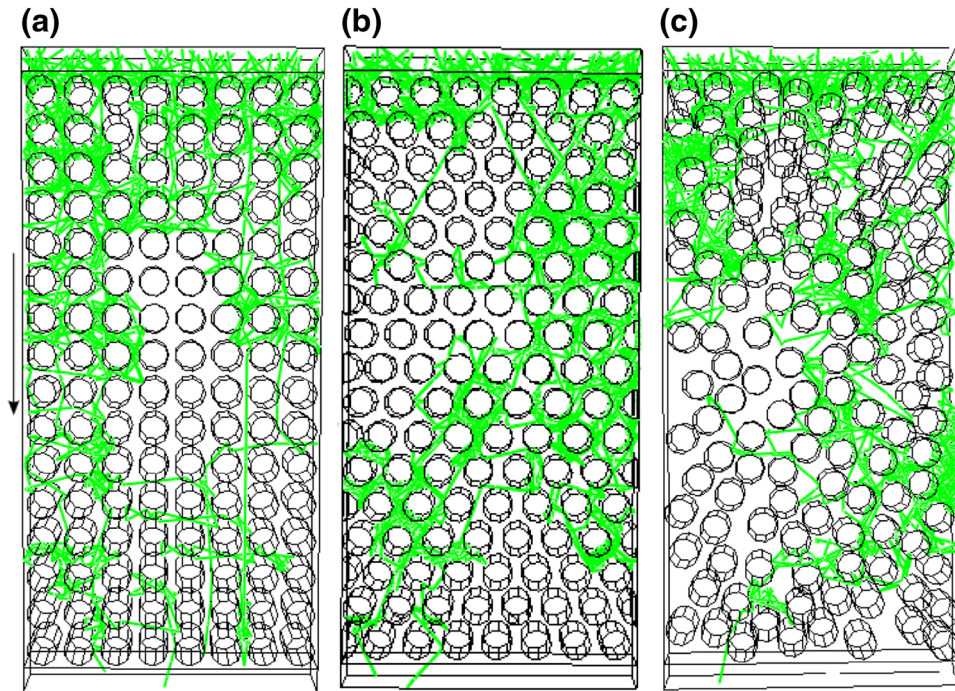


Fig. 3. Nanoporous devices with (a) rectangular, (b) hexagonal and (c) random arrangement of holes. The green lines indicate 100 trajectories of phonons, which were initialized at the top contact (source). Phonons undergo three-phonon and boundary scattering events before that reach the bottom contact (heat sink) (Color figure online).

direction, the thermal conductivity in this geometry tends to be higher than that of the hexagonal devices. Although below we only show a few phonon paths from the million paths we simulated, this behavior is representative of all phonon statistics. To quantify this, we have computed the deviation in the phonon paths along the width of the channel (i.e. the direction perpendicular to the phonon transport direction) for all phonon trajectories we simulated ($\sim 10^6$). This indicates how much the phonons deviated from the straight line going from the hot to the cold reservoir when they traveled from their point of creation to their point of thermalization. Indeed, the deviation in the hexagonal devices is larger by $\sim 20\%$, indicating that the phonons in hexagonal structures tend to spread more, or travel more in a zig-zag fashion compared to the phonons in the rectangular structure, which tend to propagate in more straight pathways. Thus, phonons in hexagonal structures tend to travel larger distances, which makes the thermal conductivity in these geometries consistently lower than the thermal conductivity in rectangular geometries and even in randomized geometries, as we show below.

The data in Fig. 4 present simulation results for the thermal conductivity in the nanomeshes examined. The thermal conductivity is plotted as a function of porosity Φ and results for structures with different boundary specular parameters are shown ($p = 1$ denotes fully specular boundaries, whereas $p = 0.1$ almost fully diffusive boundaries). In Fig. 4a, the red lines represent the results for the

nanomeshes with rectangular arrangement of the pores and the blue lines the results for the nanomeshes with hexagonal arrangement of the pores. Figure 4b shows the results for nanomeshes in which the pores are arranged randomly. In the latter case, the standard deviation is denoted by the error bars. In all cases the diameter of the pores is fixed at 50 nm. In the case of random pore arrangements, each point is the average of 100 different geometrical configurations.

Two main conclusions can be deduced from this figure. Firstly, the hexagonal and the randomized arrangements yield somewhat lower thermal conductivities compared to the rectangular ones. As explained above, this is attributed to the fact that the rectangular arrangement provides straight paths between the two reservoirs for the phonons to travel, in contrast to the other two arrangements. Secondly, as expected, the thermal conductivity decreases monotonically with increasing porosity in all three types of geometries of different pore arrangements. In the case of random pore arrangement (Fig. 4b), a smooth, linear reduction is observed with increasing porosity. As the porosity increases, the pores come closer to each other, and the MFP for pore scattering decreases in proportion to the pore separation, which linearly reduces the thermal conductivity. A similarly smooth reduction is more or less observed for the rectangular pore geometry as well (red lines in Fig. 4a). Interestingly, however, in the hexagonal pore arrangement (blue lines in Fig. 4a), and especially under diffuse phonon-boundary scattering,

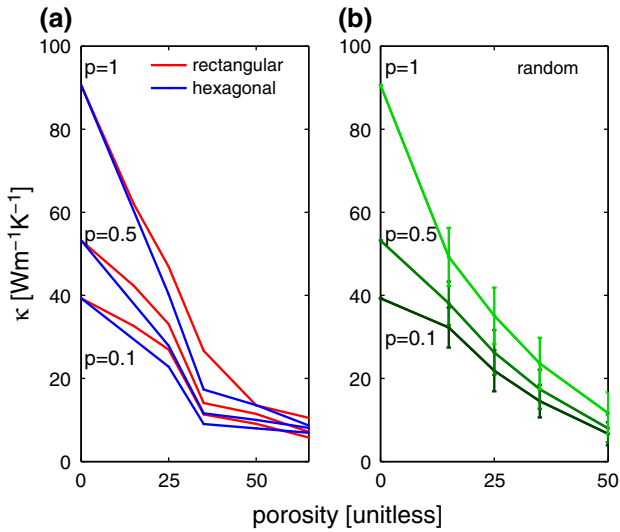


Fig. 4. The thermal conductivity as a function of porosity. Cases for pore surface roughness specularity parameter $p = 1$ (specular), $p = 0.5$ (50% specular), and $p = 0.1$ (90% diffusive) are shown. In (a) blue lines denote hexagonal pore arrangements, whereas red lines denote rectangular pore arrangements. (b) Randomized pore arrangements. 100 samples are simulated for each data point. The 'error bars' indicate the spread in the distribution of the thermal conductivity of these samples (Color figure online).

most of the reduction is observed up to a porosity of 35%. Increasing the porosity from 0% to 35% results in a factor of $\sim 4\times$ reduction in the thermal conductivity. After that, a 'knee' is observed and further increase in the porosity results in smaller relative thermal conductivity reduction. Although this effect is still under investigation, a possible explanation is that the hexagonal geometry which imposes obstacles with pores being placed directly in the phonon transport path, randomizes the phonon trajectories and scatters phonons more effectively compared to the random or rectangular arrangements, and thus the thermal conductivity is reduced more. At low porosities, all geometries have the same thermal conductivity. A stronger reduction, though, is observed for the hexagonal geometries at smaller porosities due to this stronger phonon path randomization. At larger porosities (larger than 35%), and especially for rough boundaries, it seems that phonon trajectories are randomized similarly in all geometries (the phonon MFP for scattering is similar for all, determined by the average distance between the pores), and the thermal conductivity is similar for all cases (see right sides of Fig. 4a, b). Therefore, as the starting and ending points for all geometries are the same on the thermal conductivity versus porosity figure, but the hexagonal structures reduce thermal conductivity more for smaller porosities, a 'knee' seems to form for the hexagonal structure data in Fig. 4a (blue lines). The thermal conductivity still continues to drop for porosities larger than 35%, but at a relatively smaller degree compared to structures with smaller porosities.

Specifically for the geometries consisting of randomized pores, after extracting the statistics from 100 different sample devices with random hole arrangements for each porosity value, we find that: (1) under the same porosity conditions, increasing the roughness strength by an order of magnitude (from $p = 1$ down to $p = 0.1$), reduces the thermal conductivity by only $\sim 40\%$ (see the difference between the upper and lower lines in Fig. 4b), and (2) under the same roughness conditions, it takes only 10–20% increase in the porosity to reduce the thermal conductivity by the same amount ($\sim 40\%$) (see Fig. 4b). In addition, we find that with increasing porosity the roughness strength becomes less effective in determining the thermal conductivity, indicating the relative importance of the porosity over the roughness. For example, at 50% porosity, increasing the roughness of the pores, from 50% diffusive ($p = 0.5$) to 90% diffusive ($p = 0.1$), changes the thermal conductivity only marginally.

CONCLUSIONS

In this work, we present a MC simulator for the calculation of heat transport in Si nanomeshes and a consequent study of the thermal conductivity in these structures under different geometrical constraints. We show that hexagonally arranged pores in nanomeshes can achieve lower thermal conductivities compared to rectangular arranged pores. We also show that the influence of porosity on the thermal conductivity is much stronger compared to the influence of the boundary roughness. In the case of hexagonal geometries of pore arrangement, a larger thermal conductivity reduction is observed for smaller porosities (up to 35%) compared to the rectangular or randomized pore arrangements. For largest porosities, all phonons are randomized by a similar amount, and the thermal conductivity is reduced to similar values.

ACKNOWLEDGEMENTS

This work has been supported by the Austrian Science Fund (FWF) contract P25368-N30. The authors acknowledge helpful discussions with Dr. Hossein Karamitaheri.

REFERENCES

1. J.-K. Yu, S. Mitrovic, D. Tham, J. Varghese, and J.R. Heath, *Nat. Nanotechnol.* 5, 718–721 (2010).
2. J. Tang, H.-T. Wang, D.H. Lee, M. Fardy, Z. Huo, T.P. Russell, and P. Yang, *Nano Lett.* 10, 4279–4283 (2010).
3. P.E. Hopkins, C.M. Reinke, M.F. Su, R.H. Olsson III, E.A. Shaner, Z.C. Leseman, J.R. Serrano, L.M. Phinney, and I.E. Kady, *Nano Lett.* 11, 107–112 (2011).
4. S. Mazumder and A. Majumdar, *J. Heat Transfer* 123, 749 (2001).
5. D. Lacroix, K. Joulain, and D. Lemonnier, *Phys. Rev. B* 72, 064305 (2005).
6. <http://www.globaltcad.com>. Accessed 31 July 2014.
7. M.G. Holland, *Phys. Rev.* 132, 2461–2471 (1963).

8. E. Pop, R.W. Dutton, and K.E. Goodson, *J. Appl. Phys.* 96, 4998 (2004).
9. C. Jeong, S. Datta, and M. Lundstrom, *J. Appl. Phys.* 111, 093708 (2012).
10. M.-H. Bae, Z. Li, Z. Aksamija, P.N. Martin, F. Xiong, Z.-Y. Ong, I. Knezevic, and E. Pop, *Nat. Commun.* 4, 1734 (2013).
11. K. Esfarjani, G. Chen, and H. Stokes, *Phys. Rev. B* 84, 085204 (2011).